A fluorescence-enhanced inverse opal sensing film for multi-sources detection of formaldehyde

Xiaokang Lu,[‡] Bo Han,[‡] Deyilei Wei, Mingzhu Chu, Haojie Ma, Ran Li, Xueyan Hou, Yuqi Zhang,* Ji-Jiang Wang

Key Laboratory of New Energy & New Functional Materials, Shaanxi Key Laboratory of Chemical Reaction Engineering, College of Chemistry and Chemical Engineering, Yan'an University, Yan'an, Shaanxi, 716000, P. R. China

ABSTRACT: The SiO_2 inverse opal photonic crystals (PC) with a three-dimensional macroporous structure were fabricated by the sacrificial template method, followed by infiltration of a pyrene derivative, 1-(pyren-8-yl)but-3-en-1-amine (PEA), to achieve a formaldehyde-sensitive and fluorescence-enhanced sensing film. Utilizing the specific Aza-Cope rearrangement reaction of allylamine of PEA and formaldehyde (FA) to generate a strong fluorescent product emitted at ~480 nm, we chose a PC whose blue band edge of stopband overlapped with the fluorescence emission wavelength. In virtue of the fluorescence enhancement property derived from slow photon effect of PC, FA was detected highly selectively and sensitively. The limit of detection (LoD) was calculated to be 1.38 nmol/L. Furthermore, the fast detection of FA (within 1 min) is realized due to the interconnected three-dimensional macroporous structure of the inverse opal PC and its high specific surface area. The prepared sensing film can be used for the detection of FA in air, aquatic products and living cells. The very close FA content in indoor air to the result from FA detector, the recovery rate of 101.5% for detecting FA in aquatic products and fast fluorescence imaging in 2 min for living cells demonstrate the reliability and accuracy of our method in practical applications.

Keywords: inverse opal photonic crystals, slow photon effect, fluorescence enhancement, multi-sources detection, formaldehyde

1. Introduction

Photonic crystals (PC), firstly proposed in 1987[1,2], are a kind of periodic arrangement of dielectric materials. The refractive index of PC varies periodically, endowing them with special optical properties of photonic stopband, which indicates that the light at a certain wavelength cannot transmit the materials and will be reflected. The photonic stopband character renders PC to be used in various fields, such as catalyst[3,4], solar cells[5,6], anti-counterfeiting[7,8] and sensing[9–13]. Among these applications, the PC-based sensing for external stimuli such as temperature[14,15], humidity[16], strain[17], and chemical[18–23] and biological[10,13,24–27] molecules have been paid more attention due to their regulable optical performance, for example using fluorescence enhancement effect[20,21], changeable photonic stopband position[22,23] or

Debye diffraction effect[26,27]. Presently, a variety of PC-based sensors have been developed extensively from one-dimensional PC (1DPC)[18,19], two-dimensional PC (2DPC)[26,27] to three-dimensional PC (3DPC)[20–23]. For example, a 1DPC sensor based on thiourea-functionalized nanocopolymer layer with a mesoporous TiO_2 layer for colorimetric detection of Hg^{2+}[19] has been developed. The 2DPC hydrogel aptasensors for detection of biomolecules based on measurements of Debye diffraction ring diameters[26,27] have also been reported. In addition, the 3DPC fluorescence sensors and colorimetric sensors have been developed to detect metal ions[20,21] and biomolecules[24–27]. Particularly, three-dimensional inverse opal (IO) photonic crystals with interconnected microporous structures have been widely employed to construct various sensors based on the changeable reflectance peak, such as organic solvents[22,23], explosives[28], cocaine[29] and staphylococcal enterotoxin[30]. The fluorescence sensors based on IO photonic crystals have also been developed to detect metal ions[31,32], amino acids[33], and microRNAs[34]. For example, our group have constructed highly sensitive and fast response film fluorescence sensors of Bi^{2+}[31], Fe^{3+} and Hg^{2+}[32], and cysteine[33] by combining the optical properties and the structural advantages of IO photonic crystals. The fluorescence enhancement effect arisen from the slow-photon effect of PC have been utilized to improve the detection sensitivity. The interconnected macroporous structures are beneficial to the diffusion of the analytes in the IO films and provide high specific surface area which endows the IO films with more active sites, improving the response speed. In addition, the film fluorescence analysis also has many advantages including good stability, facile operation, potential of devices fabrication, high selectivity and sensitivity. Therefore, fluorescence IO films are ideal sensing platform for various target analytes.

Aldehydes, especially formaldehyde (FA), are widely used in chemical industries, biomedicines, food and cosmetics. The extensive applications of FA bring severe threats to environments and human health because of its solubility, irritation and carcinogenicity[35,36]. Therefore, the FA detection plays an important role in ensuring air quality, food safety and human health[37,38]. For example, detecting FA is indispensable for monitoring indoor air quality because long-term exposure to high levels of FA ambient can irritate eyes, skin and even cause sore throat, headache, dyspnea and more serious leukemia[37]. In food safety, detecting FA can protect consumers' safety, prevent fraud, and avoid health risks because accidental ingestion of FA can harm reproduction and fetal development[38]. Additionally, detecting FA is also helpful for diseases prevention, early diagnosis and treatment because FA exposure in biological samples can lead to neurological issues and an increased cancer risk[37].

In present, more efforts have been dedicated on developing highly effective detection methods of FA, such as gas chromatography−mass spectrometry[39], high-performance liquid chromatography[40], surface-enhanced Raman scattering[41], electrochemical[42], colorimetric[43,44] and fluorometric[45,46] techniques. These detection techniques are sensitive, selective, and precise, but needing sophisticated instruments, trained technicians, time-consuming or having unstable signal readouts. Thereupon, in virtue of the fluorescence enhancement effect of PC films, fluorescence sensing IO films have been reported by our group for detecting FA[47,48]. However, there are still some drawbacks, such as limited application only for

gaseous FA or interference of acetaldehyde and demanded-improvement of sensitivity. Therefore, it is desirable to construct an IO fluorescence sensing film which is highly selectivity and sensitivity for FA and can be applied in FA detection from various sources including air, solution and living cells.

In this work, we constructed a pyrene derivative-infiltrated SiO_2 IO film for fast, highly selective and sensitive detection of FA in air, aquatic products and living cells. Here, SiO_2 IO was chosen due to its distinctive optical properties, structural characteristics, nontoxicity, biocompatibility, easiness of fabrication and good stability. The interconnected microporous structure of IO film facilitated the fast response and the pyrene derivative acted as a highly selective fluorescence probe of FA. The fluorescence emission was amplified by slow photon effect of PC, achieving high sensitivity of FA detection.

2. Experimental

2.1 Reagents and instruments

1-(pyren-8-yl)but-3-en-1-amine (PEA, Scheme 1) was synthesized according to the method from the literature[49] and characterized by Infrared Spectra (IR), Nuclear Magnetic Resonance Spectra (NMR) and Electrospray Ionization Mass Spectrometry (ESI-MS). The detailed synthesis process and the characterization results were shown in Supporting Information (Scheme S1 and Figure S1-S2). Monodispersed polystyrene (PS) microspheres latex (10 wt%) was acquired from Shanghai Huge Biotechnology Co., Ltd, China. Polymethyl methacrylate (PMMA, Mw = 35000) was purchased from Sinopharm Chemical Reagent Beijing Co. Ltd. Frozen squids were purchased from the local supermarket. The other analytical reagents were commercially available and used as received. Ultra–pure MilliQ water (18.2 MΩ·cm) was used for all of experiments.
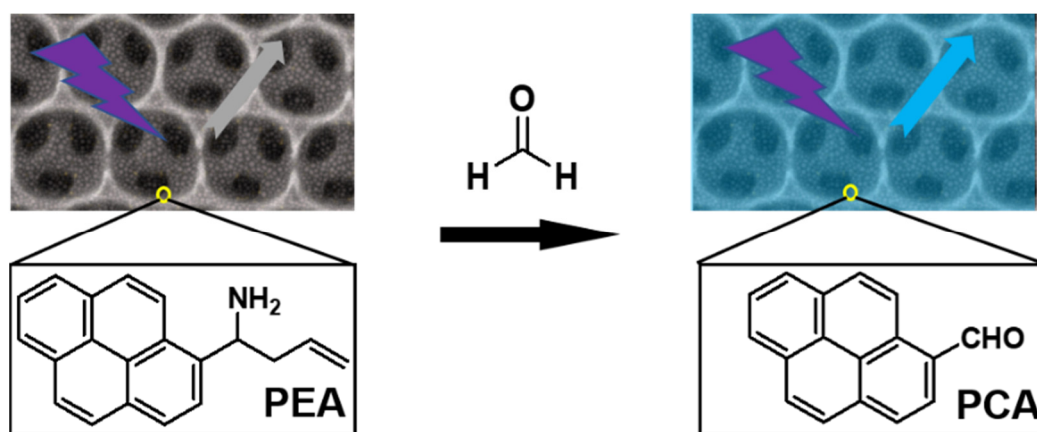
Scheme 1 Schematic illustration of IO fluorescent sensing film for FA detection.

Field emission scanning electron microscope (SEM, SU8010, Hitachi, Japan) and an atomic force microscope (AFM, Multimode 8, Bruker, Germany) were used to characterize the morphology of PCs. An optical fiber spectrophotometer (PG–2000–ProEx, Ideaoptics Instrument Co., Ltd, China) was employed to record the reflectance spectra, in which the incident light was perpendicular to the (111) plane of the PCs. The fluorescence spectra were measured by a Cary Eclipse fluorescence spectrometer (Agilent Technologies, USA), in which the film sample was placed in a quartz cuvette containing the testing

solutions and the light of 350 nm was used as excitation wavelength. Air in a decorated room was collected using a commercially multifunctional atmospheric sampler GDYK–160 (Changchun Jida Little Swan Instrument Co., Ltd., China) and FA content in air was determined by a Spectrophotometer GDYK–401RC (Changchun Jida Little Swan Instrument Co., Ltd.) The fluorescence images in HeLa cells were recorded on a LEICA DM6B fluorescence microscope.

2.2 Fabrication of IO films

We first fabricated the PS-SiO$_2$ opal PC films by co-assembly technique, followed by calcination to remove PS microspheres to acquire SiO$_2$ IO films. In detail, 20 g of monodispersed PS spheres latex at ~0.1 wt% was mixed with 0.1 mL of SiO$_2$ sol, which derived from hydrolysis of tetraethyl orthosilicate (TEOS, 28 wt%) in absolute ethanol in the presence of 0.1 M of HCl (TEOS:C$_2$H$_5$OH: HCl = 1:2:1, m:m:m)[48]. After ultrasonication for 30 min, the mixture was transferred to 5 mL of vials and clean glass slides were placed vertically. Then, the PS-SiO$_2$ opal PC films were formed at 65 °C (60% humidity) after 48 h. The resulting opal PC films were heated to 500 °C at a rate of 1 min/°C and kept at 500 °C for 3 h. The PS microspheres were removed and the three-dimensional macroporous SiO$_2$ IO films were formed, in which air microspheres were close-packed orderly in the arrangement of face-centered cubic. Various IO films with different photonic stopband were fabricated by changing the PS spheres' diameter. Here, we denoted the prepared IO films using PS spheres of 300 nm, 350 nm and 400 nm as IO$_{300}$, IO$_{350}$ and IO$_{400}$, respectively. In addition, an unordered SiO$_2$ porous film (denoted as PF$_{non}$) was also prepared using the same method, where the PS latex was composed of several different diameters of PS microspheres.

2.3 Fabrication of PEA−IO films

The PEA molecules were infiltrated into the pores of the SiO$_2$ IO films by capillary forces and adsorbed onto the pore wall. The resultant film was denoted as PEA-IO. For example, 90 µL of PEA ethanol solution (100 µmol/L) was dripped on the surface of IO$_{350}$ film (1 cm × 2.0 cm) and dried in air to give a FA-sensitive fluorescence sensing film PEA−IO$_{350}$. The infiltration content of PEA was 2.439 µg. Several PEA−IO$_{350}$ films with different PEA contents were fabricated by varying the infiltration volume of PEA solution. We also prepared a control sample PEA−PF$_{non}$ by infiltration of PEA solution (90 µL). Additionally, 90 µL of PEA tetrahydrofuran solution (100 µmol/L) containing PMMA (PEA:PMMA = 1:1, m:m) was dripped on a glass slide (1 cm × 2.0 cm) and dried to acquire a smooth PEA film as another control sample, which was marked as Glass.

2.4 Preparation of various testing solutions

Stock solutions of organic compounds: aqueous solutions (200 µmol/L) containing different organic compounds were prepared, including FA, acetaldehyde, propionaldehyde, valeraldehyde, benzaldehyde, glyoxal, benzene, toluene, acetone and ethyl acetate.

Aqueous solution of indoor air: 5 L of air collected from a decorated room using a multifunctional atmospheric sampler was slowly dissolved in 50 mL of water to be a testing solution for the detection of FA in air.

Squid extract: according to the Aquatic Industry Standard of the People's Republic of China SC/T 3025–2006[50], 10 g of the mashed squid tentacle and 20 mL of water was mixed and shaken for 30 min. After centrifugation, the supernatant was taken as the testing solution.

2.5 Cytotoxicity test and fluorescence imaging

The cytotoxicity test of PEA and its reaction product with FA toward living cells was performed using Cell Counting Kit-8 (CCK-8) assay in HeLa cells lines. Eagle mediums with 10% vol/vol of fetal bovine serum (DMEM) containing PEA (100 μmol/L) and different concentrations of FA were added to HeLa cells (37℃, 5% CO_2). The cells were incubated for 12 h and then the medium was removed, followed by washing with phosphate buffer solution (PBS, 10 mmol/L, pH = 7.4) for two times. Next, 150 μL CCK-8 (10%, vol/vol) culture medium was added and the cells were cultured for 2 h, followed by cell viability testing. Herein, the FA concentration were 0, 0.5 μmol/L ,1 μmol/L、 10 μmol/L and 50 μmol/L, respectively.

For fluorescence imaging, the Hela cells were cultured at 37 °C for 72 h on IO_{350} films, in which DMEM culture medium with 10% vol/vol of fetal bovine serum was added on the film's surface. The cells grew in the micropores and the surface of the IO_{350} films. The Hela cells grown on the surface of the IO_{350} films were washed away by rinsing with PBS for two times. The 50 μL PBS solution containing PEA (100 μmol/L) and 10 wt.% of dimethylsulfoxide (DMSO) were added to the IO_{350} films with Hela cells and remained 10 min. After washing with PBS for three times to remove PEA adsorbed on the surface of IO_{350} films, aqueous solutions of FA at concentration of 1 μmol/L and 10 μmol/L were added, respectively, and the fluorescence images were recorded at different time.

3. Results and discussion

3.1 Characterization of morphology and reflectance spectra

All the prepared PS−SiO_2 opal PC (Figure S3a−c), the corresponding IO films before (Figure S4a'−c') and after (Figure S3a"−c") infiltration of PEA, and the unordered films (Figure S3d−d") were characterized by SEM images to observe their surface morphology. The PS microspheres are close-packed orderly in the arrangement of face-centered cubic and SiO_2 nanoparticles are in the voids of PS spheres. After calcination, the resultant IO films replicated the opal PS structure perfectly, in which the PS spheres were replaced by air pores. The infiltration of PEA into the voids of SiO_2 IO films did not bring obvious morphology change compared with the original IO films due to the lower infiltration content. Figure 1a-c show SEM images of PEA−IO_{300}, PEA−IO_{350} and PEA−IO_{400}. Three dark areas can be observed in each of the air pores, demonstrating the interconnected three-dimensional microporous structure of IO film. The air pore size of the PEA−IO_{350} film is about 321 nm, which is smaller than that of the corresponding PS microsphere due to the shrinkage of SiO_2 skeleton during calcination[51]. The thickness of the PEA-IO_{350} film is about 5.9 μm

(Figure S3e). AFM image of PEA−IO$_{350}$ also confirmed this ordered macroporous structure (Figure S3f) with an average pore diameter of ~315 nm, which is consistent with the result from SEM characterization.
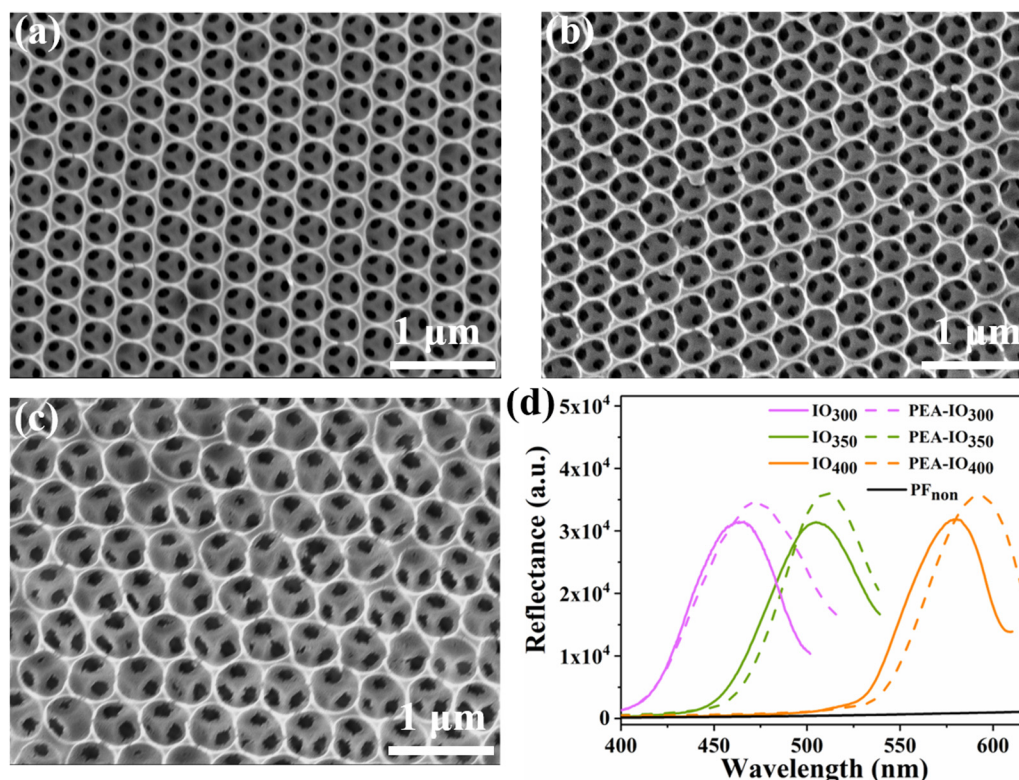

Figure 1 SEM image of (a) PEA-IO$_{300}$, (b) PEA−IO$_{350}$ and (c) PEA−IO$_{400}$. (d) The reflectance spectra of the prepared IO films before and after infiltration of PEA and the unordered SiO$_2$ porous film (PF$_{non}$).

The high orderly periodic structures of air pores endow the IO films with unique optical properties, just as the reflectance spectra demonstrated (Figure 1d). The photonic stopbands center, that is the maximum reflectance peaks, of IO$_{300}$, IO$_{350}$ and IO$_{400}$, are located at 463 nm, 504 nm and 578 nm, while red-shifted to 470 nm, 510 nm and 591 nm after infiltration of PEA, respectively. This is because the effective refractive index of the film increased slightly after the infiltration of small amount of PEA. We also can see that the unordered SiO$_2$ porous film (PF$_{non}$) does not display obvious reflectance peak compared with ordered IO films, proving the necessity of periodic structure for optical properties. The reflectance spectra of the initial PS-SiO$_2$ opal films fabricated from different diameter PS microspheres are shown in Figure S4.

3.2 Optimization of FA-sensitive IO sensing film

We chose PS microspheres with particle sizes of 300 nm, 350 nm and 400 nm as templates to prepare SiO$_2$ IO films with different photonic stopbands, followed by infiltration of ethanol solution containing PEA (100 μM, 90 μL). We immersed the resultant PEA−IO films, the control samples including the PEA−PF$_{non}$ and the smooth PEA film Glass, in 1 μmol/L of FA aqueous solution for 13 min and measured the fluorescence spectra, as presented in Figure 2a. All the films emitted fluorescence at around 480 nm. The appearance of fluorescence can be attributed to the Aza−Cope arrangement reaction between PEA and FA[49], which formed a fluorescent product pyrene-1-carbaldehyde (PCA), as shown in Scheme 1.
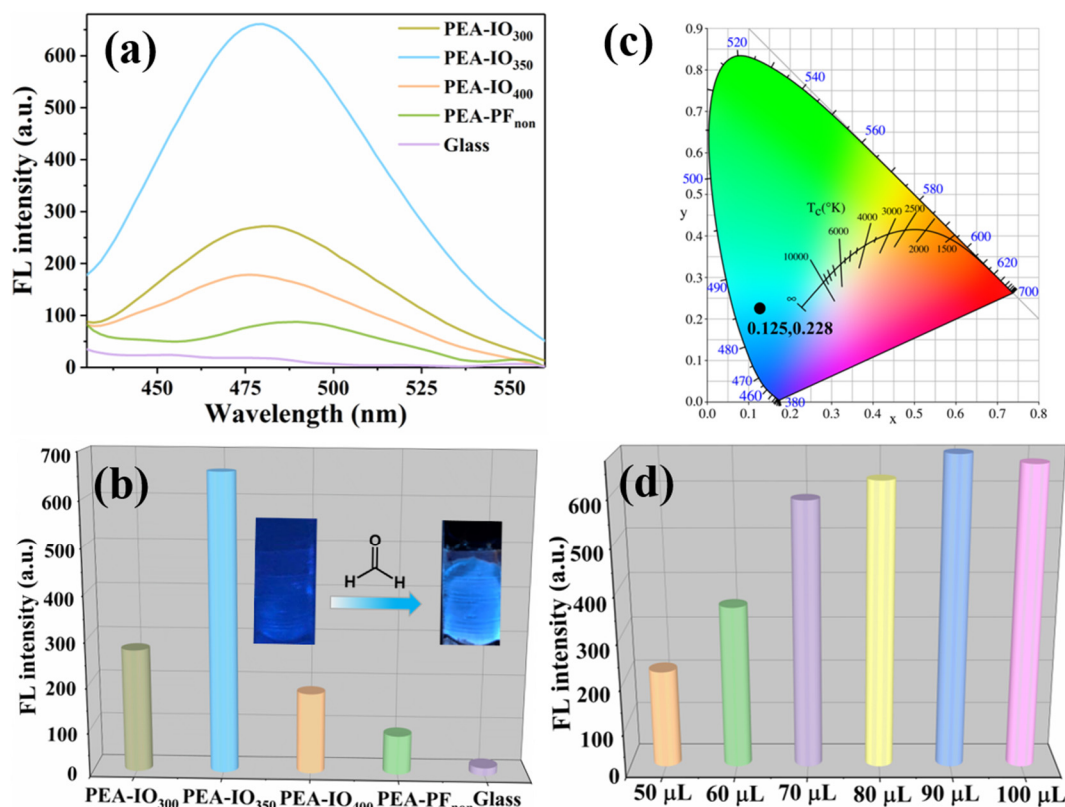
Figure 2 (a) Fluorescence (FL) spectra of PEA−infiltrated IO films and the control sample Glass upon exposure to 1 **µmol/L of FA aqueous solution.** (b) The corresponding fluorescence intensity at maximum emission wavelength. **Inset: photographs of PEA−IO₃₅₀ before and after response to FA (taken under UV light of 365 nm). (c) CIE chromaticity diagram for fluorescence spectrum of PEA−IO₃₅₀. (d)** Fluorescence intensity (at ~480 nm) of different PEA−**IO₃₅₀ by adjusting infiltration volume of PEA ethanol solution when immersed in 1 µmol/L of FA aqueous solution. (λ_{ex} = 350 nm).**

Figure 2b exhibits the fluorescence intensity of the different films containing PEA in the FA solution. Obviously, the films with porous structure exhibited stronger fluorescence than that of the control sample Glass and the PEA−IO₃₅₀ film has the strongest fluorescence. There was a 38.7-times increase in fluorescence intensity for PEA−IO₃₅₀ film compared with that of Glass. The remarkable fluorescence enhancement is arisen from the slow photon effect endowed by PC[52], in which the emission wavelength of the reaction product PCA (~480 nm) overlapped with the blue-band edge of the photonic stopband of PEA−IO₃₅₀ film (Fig. 1b). Here, the photon group velocity becomes slow and the resultant high density of states enhances the coupling of photons to the local resonance mode, further enhancing the interaction between light and matter, and ultimately improving the efficiency of photocarrier generation, thus generating a fluorescence amplification effect[53,54]. The strongest fluorescence occurred for the PEA−IO₃₅₀ film because the reaction product PCA is a low refractive index material[55] which shows stronger interaction with light at blue band edge of the photonic stopband[56]. The other films containing three-dimensional microporous structures show a certain fluorescence enhancement compared with that of Glass due to their higher specific surface area than smooth PEA film (Glass). Therefore, in the subsequent experiments, we chose PEA−IO₃₅₀ as the optimal PC film for FA detection.

The photographs (Inset in Figure 2b) of the PEA−IO₃₅₀ film before and after immersion in the FA solution were taken under UV irradiation of 365 nm. We can observe that the film did not emit fluorescence

before exposure to FA solution, while it emitted cyan fluorescence after contacting FA. Figure 2c shows the CIE1931 chromaticity diagram plotted from the fluorescence spectrum (Figure 2a) of PEA−IO$_{350}$ film in FA solution. The coordinate point of the fluorescence appeared at (0.125, 0.228), displaying cyan color. The result is consistent with the observed fluorescence color from the photograph. As depicted in Scheme 1, PEA molecules were infiltrated into the voids of SiO$_2$ IO films and adsorbed on the pore walls. There is no fluorescence emission for the initial PEA−IO film. Upon exposure to FA environment, the IO film shows obvious cyan fluorescence under UV light because PEA reacts with FA to generate a fluorescent product PCA which emit fluorescence at around 480 nm. Furthermore, the fluorescence intensity can be enhanced significantly due to the slow photon effect derived from PC. Thus, the as-constructed PEA−IO film can be employed as a "turn−on" fluorescent sensing film for the determination of FA.

The IO$_{350}$ film was used as the sensing film candidate to prepare PEA−IO$_{350}$ films containing different contents of PEA by dripping different volumes of PEA ethanol solution of 100 μmol/L. The resultant PEA−IO$_{350}$ films were exposed to the 1 μmol/L of FA solution for 13 min, followed by fluorescence measurement. Figure 2d presents the fluorescence intensity of these PEA−IO$_{350}$ films at ~480 nm and the corresponding spectra are shown in Figure S5. Clearly, the fluorescence increased gradually when the volume of PEA solution changed from 50 μL to 90 μL and finally achieved to a maximum value. This is because the more PEA in the IO film, the more fluorescence product PCA formed. Therefore, the PEA−IO$_{350}$ film prepared from 90 μL of PEA solution was chosen as the optimized IO sensing film to investigate the detection performance to FA.

## 3.3 Detection of FA using PEA−IO$_{350}$ sensing film

The PEA-IO$_{350}$ film was immersed in 1 μmol/L of FA solution and the fluorescence spectra at different immersion time were recorded, as shown in Figure 3a. The fluorescence can be observed after immersion for 1 min. The fast response to FA is because the interconnected macroporous structure of the IO sensing film is conducive to the rapid diffusion of FA molecules, and its high specific surface area offers more active reaction sites. The fluorescence intensity (Figure 3b) gradually enhanced as the immersion time increased. The intensity reached to a level after the IO sensing film reacted with FA for 13 min. Therefore, the following fluorescence were measured after the sensing film was exposed to the solution for 13 min.
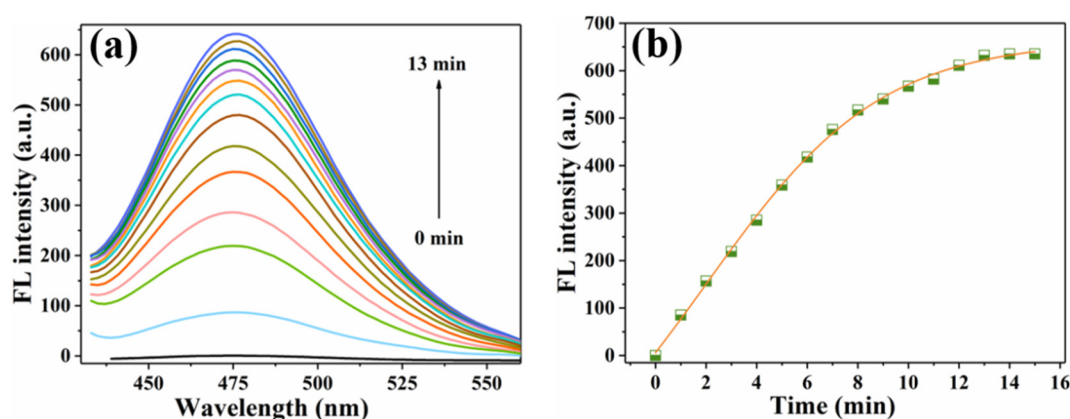
Figure 3 Time dependence of (a) fluorescence spectra and (b) the intensity (at ~480 nm) of PEA−**IO$_{350}$ film after immersion in 1 μmol/L of FA aqueous solution. (λ$_{ex}$ = 350 nm).**

The fluorescence spectra dependence of PEA−IO$_{350}$ film on FA concentration were given in Figure 4a, which was used to investigate the limit of detection (LoD) of the sensing film to FA. The fluorescence intensity increased with increasing the FA concentrations and reached to a level until the concentration increased to 900 nmol/L. The fluorescence intensity showed a good linear relationship with R^2 = 0.9936 towards the FA concentration when it varied from 50 nmol/L to 600 nmol/L (Figure 4b). The LoD of 1.38 nmol/L for FA detection was acquired according to the formula LoD = 3σ/s, where σ is the standard deviation of blank measurement and s is the slope of the calibration curve. The results demonstrate that the sensing film has a higher sensitivity compared with that of other materials based on fluorimetric technique (Table S1), and the LoD also improved two orders of magnitude compared with that from the PEA solution system[49]. Furthermore, compared with the sensors based on the IO film using electrical signal to sense, the FA detection of our constructed IO film shows better selectivity, lower detection temperature (at room temperature, not needing high temperature) and multi-sources FA including gaseous state[57].
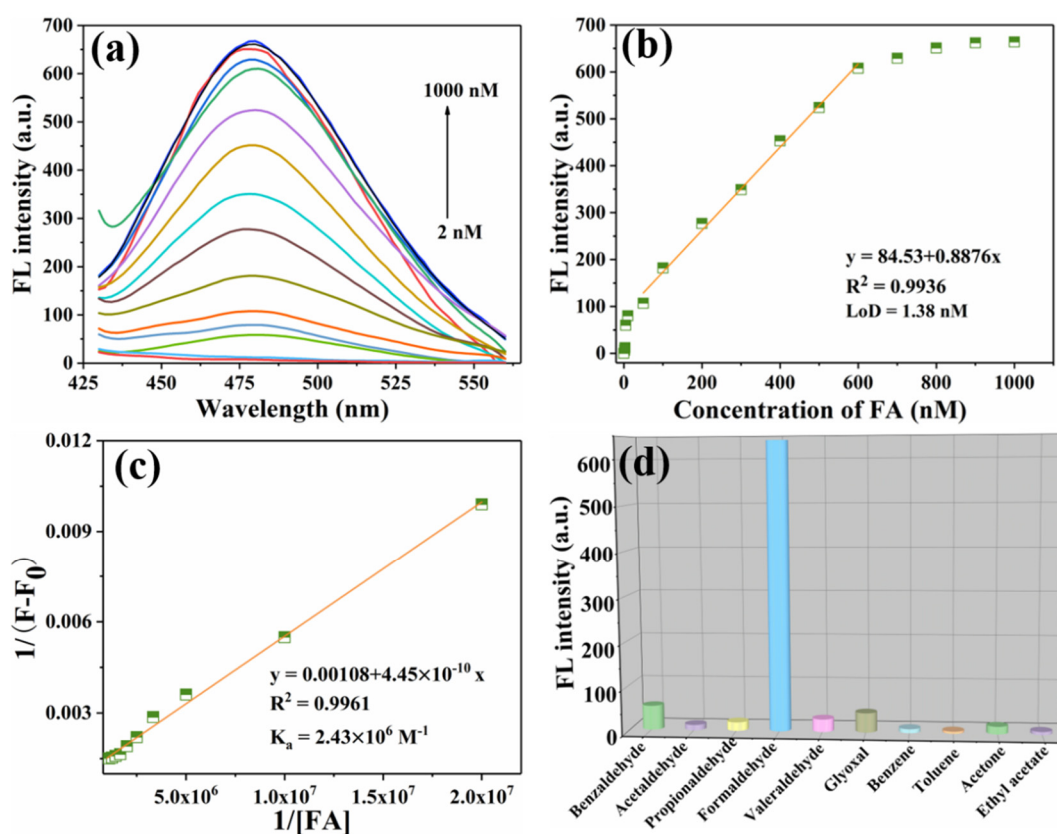
Figure 4 Dependence of (a) fluorescence spectra and (b) intensity (at ~480 nm) for PEA−**IO$_{350}$** on FA concentrations. (c) Benesi–Hildebrand plot of PEA−**IO$_{350}$** for FA. (d) Fluorescence intensity (at ~480 nm) of PEA−**IO$_{350}$** after exposure to aqueous solutions (1 **μmol/L**) containing different organic compounds.

The Benesi–Hildebrand theory[58] was used to deduce the interaction ability between the PEA−IO$_{350}$ film and FA. The fluorescence [1/(F − F$_0$)] was plotted against 1/[FA] according to the following Benesi–Hildebrand Equation, as shown in Figure 4c.

$$\frac{1}{F - F_0} = \frac{1}{K_a(F_{max} - F_0)[FA]} + \frac{1}{(F_{max} - F_0)}$$

Here, F_0 and F are the fluorescence intensity of PEA−IO$_{350}$ film before and after exposure to FA solution, and F_{max} is the maximum intensity in FA solution. [FA] represents the concentration of FA solution and K_a represents interaction ability between the PEA−IO$_{350}$ film and FA. Figure 4c gives a good linear correlation (R^2 = 0.9961) and the K_a was determined to be 2.43×10^6 M^{-1}, indicating a strong interaction between PEA−IO$_{350}$ film and FA molecules. Figure 4d provides the fluorescence intensity (at ~480 nm) of the PEA−IO$_{350}$ film upon exposure to different organic compounds aqueous solutions (1 μmol/L). The fluorescence spectra in different solutions are given in Figure S6. It can be seen that the sensing film displayed the strongest fluorescence intensity when placed in FA solution, in which the intensity was nearly 50-fold compared with those in other compounds solutions. The results demonstrated that the constructed PEA−IO$_{350}$ film is a highly selective sensor for the detection of FA, which is based on the excellent and specific Aza-Cope rearrangement reaction between PEA and FA[49].

3.4 Application of FA detection using PEA−IO$_{350}$ sensing film

We first tried to detect FA in indoor air. The PEA−IO$_{350}$ sensing film was placed in the aqueous solution containing the air collected from a new-decorated room, followed by fluorescence measurement. The resultant fluorescence spectrum is shown in Figure 5a. We measured 5 parallel samples of indoor air solution and averaged the fluorescence intensity, as shown in Table S2. According to the linear relationship between the fluorescence intensity and FA concentration (Figure 4b), y = 0.8876x+84.53, we calculated the FA content in the air solution to be 283.91 nmol/L. Then, we can obtain the FA concentration ($C_{FA\ in\ air}$) in the collected indoor air to be 0.085 mg·m^{-3} based on the following calculation. In addition, the FA concentration in air of this decorated room was measured by a commercial FA detector to be 0.08 mg·m^{-3} (Figure S7). The result from our method was very close to that from the FA detector, testifying the accuracy of this sensing film for monitoring FA in air.

$$C_{FA\ in\ air} = \frac{283.91\,nM \times 10^{-9} \times 50\ mL \times 10^{-3} \times 30\ g/mol \times 10^3}{5\ L \times 10^{-3}} = 0.085\ mg/m^3$$

Detection of FA in the aquatic products was also utilized to evaluate the application performance of the PEA−IO$_{350}$ sensing film. The sensor showed an obvious fluorescence emission upon exposure to the original squid extract (green line in Figure 5). Similarly, the FA content was found to be 240.60 nmol/L via the linear correlation between the fluorescence intensity and FA concentration. As a comparison, we prepared an aqueous solution containing 241 nmol/L of FA as testing solution. The fluorescence spectrum (orange line in Figure 5) which is nearly agreement with that of the original squid extract demonstrated the detection accuracy of this sensor. Additionally, we also added 100 nmol/L of FA to the original extract, followed by and fluorescence measurement and FA concentration calculation. The calculated FA concentration was 342.11 nmol/L and the recovery rate of 101.5% was acquired, further confirming the reliability and accuracy of our constructed PEA−IO$_{350}$ sensing film for detecting FA in aquatic products.
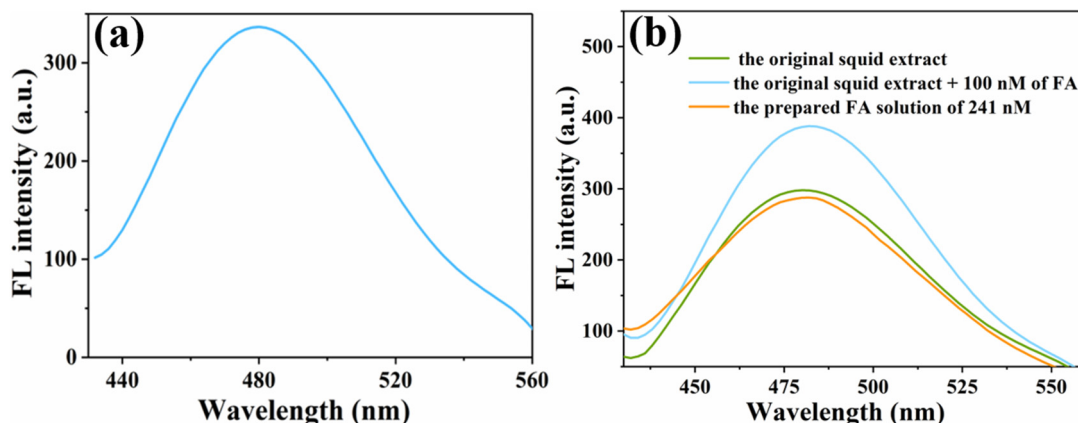
Figure 5 Fluorescence spectra of PEA−IO_{350} immersed in various aqueous solutions: (a) aqueous solution of indoor air collected from a decorated room; (b) the original squid extract, the solution after adding 100 nmol/L of FA and the prepared FA solution of 241 nmol/L.

The fluorescence imaging was performed in living cells to extend the FA detection and its biomarker application. The viability of HeLa cells was studied in the presence of PEA and different concentrations of FA, as shown in Figure S8. The cell viability was 95% for PEA and around 70% when 50 μmol/L of FA was added. The HeLa cells in the IO_{350} film containing PEA did not emit fluorescence (Figure 6a and 6a'). However, blue fluorescence could be observed obviously after FA was added. Figures 6b-f show the fluorescence images of the HeLa cells in the presence of 1 μmol/L FA. We can find the blue fluorescence occurred in 2 min and became brighter at longer observation time, demonstrating a fast response. The fluorescence was stronger and the image became brighter at the same observation time when FA was 10 μmol/L (Figure 6b'-f'). The results indicated that our constructed PEA−IO_{350} films are a good candidate for determining FA and bioimaging of living cells, showing potential clinical testing application.
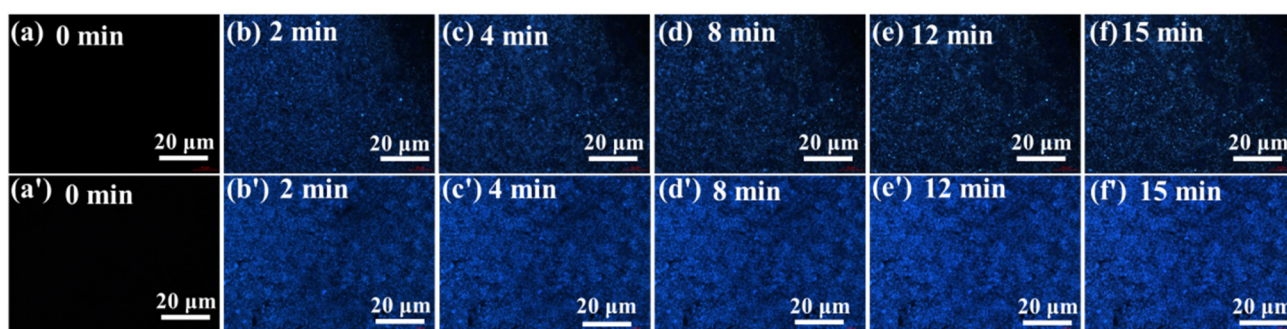
Figure 6 Fluorescence images of HeLa cells incubated on the surface of IO_{350} film containing PEA after adding (a–f) 1 μmol/L and (a'–f') 10 μmol/L of FA at different time.

4. Conclusions

The SiO_2 inverse opal photonic crystal infiltrated by PEA was employed as a fluorescence enhancement sensing film for rapid and highly sensitive detection of formaldehyde. The no-fluorescence PEA underwent a chemoselective Aza−Cope rearrangement reaction with FA to generate a fluorescent product PCA emitted at ~480 nm, constructing a "turn-on" fluorescence sensing film with high selectivity. The slow photon effect of PC based on the matching of blue-band edge of the photonic stopband and the emission wavelength remarkably enhanced the fluorescence intensity of the film, improving the detection sensitivity (LoD, 1.38 nmol/L) of FA two orders of magnitude compared with solution system. The interconnected porous structure

and high specific surface area of the inverse opal rendered the film a rapid response within 1 min. The constructed PEA−IO$_{350}$ sensing film was successfully applied in the detection of FA in indoor air, squid extract and living cells. The FA content in indoor air was very close to that from the FA detector, and the recovery rate of 101.5% was achieved for detecting FA in squid extract. The fluorescence imaging could be observed in 2 min for living HeLa cells. The results demonstrated that the as-constructed PEA−IO can be an excellent fluorescence sensing film for selective, sensitive and fast determination of FA in air, aquatic products and biological cells. Our method can be extended to design different functional molecules infiltrated inverse opal films for detection of various analytes.

Conflicts of interest

There are no conflicts to declare.

Acknowledgement

References

[1] E. Yablonovitch, Inhibited spontaneous emission in solid-state physics and electronics, Phys. Rev. Lett. 58 (1987) 2059–2062. https://doi.org/10.1103/PhysRevLett.58.2059.

[2] S. John, Strong localization of photons in certain disordered dielectric superlattices, Phys. Rev. Lett. 58 (1987) 2486–2489. https://doi.org/10.1103/PhysRevLett.58.2486.

[3] S.Y. Lim, C.S. Law, M. Markovic, et al., Engineering the slow photon effect in photoactive nanoporous anodic alumina gradient-index filters for photocatalysis, ACS Appl. Mater. Interfaces. 10 (2018) 24124–24136. https://doi.org/10.1021/acsami.8b05946.

[4] S.Y. Lim, C.S. Law, M. Markovic, et al., Rational management of photons for enhanced photocatalysis in structurally-colored nanoporous anodic alumina photonic crystals, ACS Appl. Energy Mater. 2 (2019) 1169–1184. https://doi.org/10.1021/acsaem.8b01721.

[5] S. Almenabawy, Y. Zhang, A. Flood, et al., Nanometer-mesa inverted-pyramid photonic crystals for thin silicon solar cells, ACS Appl. Energy Mater. 5 (2022) 13808–13816. https://doi.org/10.1021/acsaem.2c02437.

[6] N. Daem, A. Mayer, G. Spronck, et al., Inverse opal photonic nanostructures for enhanced light harvesting in CH$_3$NH$_3$PbI$_3$ perovskite solar cells, ACS Appl. Nano Mater. 5 (2022) 13583–13593. https://doi.org/10.1021/acsanm.2c03274.

[7] K. Chen, Y. Zhang, J. Ge, Highly invisible photonic crystal patterns encrypted in an inverse opaline macroporous polyurethane film for anti-counterfeiting applications, ACS Appl. Mater. Interfaces. 11 (2019) 45256–45264. https://doi.org/10.1021/acsami.9b18995.

[8] Z. Tian, Z. Zhang, D. Zhang, et al., Transparent encryption of nanostructured photonic patterns by erasing the structural colors of visible patterns: implications for anti-counterfeiting and information encryption applications, ACS Appl. Nano Mater. 5 (2022) 12787–12796. https://doi.org/10.1021/acsanm.2c02679.

[9] F. Fathi, M.-R. Rashidi, P.S. Pakchin, et al., Photonic crystal based biosensors: emerging inverse opals for biomarker detection, Talanta. 221 (2021) 121615. https://doi.org/10.1016/j.talanta.2020.121615.

[10] Y. Foelen, A.P.H.J. Schenning, Optical indicators based on structural colored polymers, Sci. Adv. 9 (2022) 2200399. https://doi.org/10.1002/advs.202200399.

[11] J. Wang, P.W.H. Pinkse, L.I. Segerink, et al., Bottom-up assembled photonic crystals for structure-enabled label-free sensing, ACS Nano. 15 (2021) 9299–9327. https://doi.org/10.1021/acsnano.1c02495.

[12] X. Du, J. Zhai, X. Li, et al., Hydrogel-based optical ion sensors: principles and challenges for point-of-care testing and environmental monitoring, ACS Sens. 6 (2021) 1990–2001. https://doi.org/10.1021/acssensors.1c00756.

[13] P. Shen, Y. Zhang, Z. Cai, et al., Three-dimensional/two-dimensional photonic crystal hydrogels for biosensing, J. Mater. Chem. C. 9 (2021) 5840–5857. https://doi.org/10.1039/D1TC00830G.

[14] L. Cai, Y. Wang, L. Sun, et al., Bio-inspired multi-responsive structural color hydrogel with constant volume and wide viewing angles, Adv Opt Mater. 9 (2021) 2100831. https://doi.org/10.1002/adom.202100831.

[15] F. Liu, S. Zhang, X. Jin, et al., Thermal-responsive photonic crystal with function of color switch based on thermochromic system, ACS Appl. Mater. Interfaces. 11 (2019) 39125–39131. https://doi.org/10.1021/acsami.9b16411.

[16] D. Kou, W. Ma, S. Zhang, et al., High-performance and multifunctional colorimetric humidity sensors based on mesoporous photonic crystals and nanogels, ACS Appl. Mater. Interfaces. 10 (2018) 41645–41654. https://doi.org/10.1021/acsami.8b14223.

[17] P. Snapp, P. Kang, J. Leem, et al., Colloidal photonic crystal strain sensor integrated with deformable graphene phototransducer, Adv. Funct. Mater. 29 (2019) 1902216. https://doi.org/10.1002/adfm.201902216.

[18] R.M. Caraballo, D. Onna, N. López Abdala, et al., Metalloporphyrins into mesoporous photonic crystals: towards molecularly-tuned photonic sensing devices, Sens. Actuators B Chem. 309 (2020) 127712. https://doi.org/10.1016/j.snb.2020.127712.

[19] D. Kou, W. Ma, S. Zhang, Functionalized mesoporous photonic crystal film for ultrasensitive visual detection and effective removal of mercury (ii) ions in water, Adv. Funct. Mater. 31 (2021) 2007032. https://doi.org/10.1002/adfm.202007032.

[20] L. Zhang, B. Liu, W. Yang, et al., Laser-induced patterned photonic crystal heterostructure for multimetal ion recognition, ACS Appl. Mater. Interfaces. 13 (2021) 4330–4339. https://doi.org/10.1021/acsami.0c18500.

[21] Y. Huang, L. Liu, X. Yang, et al., A diverse micromorphology of photonic crystal chips for multianalyte sensing, Small. 17 (2021) 2006723. https://doi.org/10.1002/smll.202006723.

[22] D. Yan, L. Qiu, K.J. Shea, et al., Dyeing and functionalization of wearable silk fibroin/cellulose composite by nanocolloidal array, ACS Appl. Mater. Interfaces. 11 (2019) 39163–39170. https://doi.org/10.1021/acsami.9b11576.

[23] M. Guo, X.-Q. Yu, J. Zhao, et al., Versatile titanium dioxide inverse opal composite photonic hydrogel films towards multi-solvents chip sensors, Sens. Actuators B Chem. 347 (2021) 130639. https://doi.org/10.1016/j.snb.2021.130639.

[24] J. Qin, X. Li, L. Cao, et al., Competition-based universal photonic crystal biosensors by using antibody–antigen interaction, J. Am. Chem. Soc. 142 (2020) 417–423. https://doi.org/10.1021/jacs.9b11116.

[25] D. Lu, M. Qin, Y. Zhao, et al., Supramolecular photonic hydrogel for high-sensitivity alkaline phosphatase detection via synergistic driving force, Small. 19 (2023) 2206461. https://doi.org/10.1002/smll.202206461.

[26] P. Shen, M. Li, R. Li, et al., Aptamer-functionalized smart photonic hydrogels: application for the detection of thrombin in human serum, NPG Asia Mater. 14 (2022) 1–12. https://doi.org/10.1038/s41427-022-00443-y.

[27] C. Liu, W. Zhang, Y. Zhao, et al., Urea-functionalized poly(ionic liquid) photonic spheres for visual identification of explosives with a smartphone, ACS Appl. Mater. Interfaces. 11 (2019) 21078–21085. https://doi.org/10.1021/acsami.9b04568.

[28] P. Shen, K. Jang, Z. Cai, et al., Aptamer-functionalized 2D photonic crystal hydrogels for detection of adenosine, Microchim Acta. 189 (2022) 418. https://doi.org/10.1007/s00604-022-05521-0.

[29] S. Wang, Y. Qi, Q. Chen, et al., Control of liquid crystal microarray optical signals using a microspectral mode based on photonic crystal structures, Anal. Chem. 93 (2021) 11887–11895. https://doi.org/10.1021/acs.analchem.1c02920.

[30] H. Shen, J. Bai, X. Zhao, et al., Highly ordered, plasmonic enhanced inverse opal photonic crystal for ultrasensitive detection of staphylococcal enterotoxin B, ACS Appl. Mater. Interfaces. 14 (2022) 4637–4646. https://doi.org/10.1021/acsami.1c18386.

[31] Y. Zhang, Q. Li, P. Guo, et al., Fluorescence-enhancing film sensor for highly effective detection of Bi^{3+} ions based on SiO_2 inverse opal photonic crystals, J. Mater. Chem. C. 6 (2018) 7326–7332. https://doi.org/10.1039/C8TC01461B.

[32] Y. Zhang, X. Li, L. Gao, et al., Silole-infiltrated photonic crystal films as effective fluorescence sensor for Fe^{3+} and Hg^{2+}, ChemPhysChem. 15 (2014) 507–513. https://doi.org/10.1002/cphc.201300949.

[33] H. Li, B. Han, H. Ma, et al., A "turn-on" inverse opal photonic crystal fluorescent sensing film for detection of cysteine and its bioimaging of living cells, Microchim Acta. 190 (2023) 49. https://doi.org/10.1007/s00604-022-05627-5.

[34] Y. Xu, H. Wang, C. Luan, et al., Porous hydrogel encapsulated photonic barcodes for multiplex microRNA quantification, Advanced Functional Materials. 28 (2018) 1704458. https://doi.org/10.1002/adfm.201704458.

[35] T. Salthammer, S. Mentese, R. Marutzky, Formaldehyde in the indoor environment, Chem. Rev. 110 (2010) 2536–2572. https://doi.org/10.1021/cr800399g.

[36] H. Reingruber, L.B. Pontel, Formaldehyde metabolism and its impact on human health, Curr. Opin. Toxicol. 9 (2018) 28–34. https://doi.org/10.1016/j.cotox.2018.07.001.

[37] L. Zhang, C. Steinmaus, D.A. Eastmond, et al., Formaldehyde exposure and leukemia: a new meta-analysis and potential mechanisms, Mutat. Res.-Rev. Mutat. 681 (2009) 150–168. https://doi.org/10.1016/j.mrrev.2008.07.002.

[38] P. Restani, C. Galli, Oral toxicity of formaldehyde and its derivatives, Crit. Rev. Toxicol. 21(1991) 315–328. https://doi.org/10.3109/10408449109019569.

[39] T.-S. Yeh, T.-C. Lin, C.-C. Chen, et al., Analysis of free and bound formaldehyde in squid and squid products by gas chromatography–mass spectrometry, J Food Drug Anal. 21 (2013) 190–197. https://doi.org/10.1016/j.jfda.2013.05.010.

[40] P.-W. Wu, C.-C. Chang, S.-S. Chou, Determination of formaldehyde in cosmetics by HPLC method and acetylacetone method, J Food Drug Anal. 11 (2020). https://doi.org/10.38212/2224-6614.2728.

[41] Q. Liu, X. Zeng, Y. Tian, et al., Dynamic reaction regulated surface-enhanced Raman scattering for detection of trace formaldehyde, Talanta. 202 (2019) 274–278. https://doi.org/10.1016/j.talanta.2019.05.004.

[42] D. Fu, T. Chen, Y. Cheng, et al., A molecularly imprinted electrochemical sensing platform based on the signal amplification system fabricated with the theoretically optimized monomer for specific determination of formaldehyde, Sens. Actuators B Chem. 344 (2021) 130260. https://doi.org/10.1016/j.snb.2021.130260.

[43] M. Li, A. Shen, Y. Hou, et al., Biomimetic enzyme MOF-NADH-mediated and 3,3′,5,5′-tetramethylbenzidine-based colorimetric assay for formaldehyde detection, Sens. Actuators B Chem. 366 (2022) 132007. https://doi.org/10.1016/j.snb.2022.132007.

[44] K. Kaewnu, S. Boonna, S. Kongkaew, et al., A portable colorimetric device based on PVDF indicator gel for formaldehyde detection in food and wood products, Microchem. J. 184 (2023) 108162. https://doi.org/10.1016/j.microc.2022.108162.

[45] X. Zhao, C. Ji, L. Ma, et al., An aggregation-induced emission-based "turn-on" fluorescent probe for facile detection of gaseous formaldehyde, ACS Sens. 3 (2018) 2112–2117. https://doi.org/10.1021/acssensors.8b00664.

[46] A. Hou, H. Chen, C. Zheng, et al., Assembly of a fluorescent chiral photonic crystal membrane and its sensitive responses to multiple signals induced by small molecules, ACS Nano. 14 (2020) 7380–7388. https://doi.org/10.1021/acsnano.0c02883.

[47] Y. Zhang, L. Mu, R. Zhou, et al., Fluoral-p infiltrated SiO_2 inverse opal photonic crystals as fluorescent film sensors for detecting formaldehyde vapor, J. Mater. Chem. C. 4 (2016) 9841–9847. https://doi.org/10.1039/C6TC03862J.

[48] X. Lu, R. Li, B. Han, et al., Fluorescence sensing of formaldehyde and acetaldehyde based on responsive inverse opal photonic crystals: a multiple-application detection platform, ACS Appl. Mater. Interfaces. 13 (2021) 13792–13801. https://doi.org/10.1021/acsami.0c22105.

[49] D. Zhang, D. Liu, M. Li, et al., A simple pyrene-based fluorescent probe for highly selective detection of formaldehyde and its application in live-cell imaging, Anal. Chim. Acta. 1033 (2018) 180–184. https://doi.org/10.1016/j.aca.2018.05.065.

[50] Aquatic Industry Standard of the People's Republic of China. SC/T 3025-2006.

[51] Y.Q. Zhang, J.X. Wang, X. Chen, et al., Enhancing fluorescence of tricolor fluorescent powders by silica inverse opals, Appl. Phys. A. 87 (2007) 271–275. https://doi.org/10.1007/s00339-006-3830-7.

[52] T. Baba, Slow light in photonic crystals, Nat. Photonics. 2 (2008) 465–473. https://doi.org/10.1038/nphoton.2008.146.

[53] V.I. Kopp, B. Fan, H.K.M. Vithana, et al., Low-threshold lasing at the edge of a photonic stop band in cholesteric liquid crystals, Opt. Lett. 23 (1998) 1707–1709. https://doi.org/10.1364/OL.23.001707.

[54] M. Zelsmann, E. Picard, T. Charvolin, et al., Seventy-fold enhancement of light extraction from a defectless photonic crystal made on silicon-on-insulator, Appl. Phys. Lett. 83 (2003) 2542–2544. https://doi.org/10.1063/1.1614832.

[55] H. Li, J. Wang, Z. Pan, et al. Amplifying fluorescence sensing based on inverse opal photonic crystal toward trace TNT detection, J. Mater. Chem. 21 (2011) 1730–1735. https://doi.org/10.1039/C0JM02554B.

[56] S. Nishimura, N. Abrams, B.A. Lewis, et al., Standing wave enhancement of red absorbance and photocurrent in dye-sensitized titanium dioxide photoelectrodes coupled to photonic crystals, J. Am. Chem. Soc. 125 (2003) 6306–6310. https://doi.org/10.1021/ja034650p.

[57] R. Xing, L. Xu, Y. Zhu, et al., Three-dimensional ordered SnO_2 inverse opals for superior formaldehyde gas-sensing performance, Sens. Actuators B Chem. 188 (2013) 235–241. http://dx.doi.org/10.1016/j.snb.2013.07.024.

[58] H.A. Benesi, J.H. Hildebrand, A spectrophotometric investigation of the interaction of iodine with aromatic hydrocarbons, J. Am. Chem. Soc. 71 (1949) 2703–2707. https://doi.org/10.1021/ja01176a030.